Biosensors and Bioelectronics: X 28 (2026) 100733

Contents lists available at ScienceDirect

Biosensors and Bioelectronics: X

journal homepage: www.journals.elsevier.com/biosensors-and-bioelectronics-x

A machine learning framework for advanced analytical detection of CD36 using immunosensors below limit of detection ☆

Muhammet Cagri Yeke [a], Sultan Sacide Gelen [b], Hilal Fil [b], Muhammet Mustafa Yalcin [b], Abdurrahman Gumus [c,*], Idris Yazgan [d], Dilek Odaci [b,*]

[a] Department of Biotechnology and Bioengineering, Izmir Institute of Technology, Urla, Izmir, 35430, Turkey
[b] Department of Biochemistry, Ege University, Bornova, Izmir, 35040, Turkey
[c] Department of Computer Engineering, Isparta University of Applied Sciences, Merkez, Isparta, 35430, Turkey
[d] Department of Biology, Kastamonu University, Merkez, Kastamonu, 37200, Turkey

ARTICLE INFO

Dataset link: https://github.com/miralab-ai/biosensors-AI

Keywords:
CD36
Biosensor
Regression
Machine learning
Augmentation

ABSTRACT

We introduce a machine learning (ML)-based regression framework for quantitative electrochemical analysis, representing a paradigm shift from traditional univariate methods to a multivariate approach. Conventional analysis is constrained by reducing the entire signal to a single peak current feature to define a linear range and calculate a limit of detection (LOD). In contrast, our methodology treats the Differential Pulse Voltammetry (DPV) curve as time-series data, creating a high-dimensional fingerprint by systematically evaluating multiple data windows with varying widths around the main signal peak to identify the most informative segment. To validate this approach, a biosensor was developed by immobilizing Anti-CD36 antibodies on polydopamine-modified screen-printed carbon electrodes for the detection of CD36, a key protein in metabolism and immunity. Measurements were collected across 12 concentrations, including blank samples, spanning a range of 0 to 25 ng/mL. Following data augmentation, nine different regression models were evaluated, with the top-performing models achieving near-perfect prediction accuracy ($R^2 > 0.99$) across this entire range. This high accuracy across the full concentration spectrum quantitatively demonstrates the method's ability to operate without relying on traditional concepts like linear range or LOD, enabling reliable detection at ultra-low levels. Furthermore, the immunosensor exhibited high selectivity against common interferents and excellent recovery in human serum. This methodology represents a significant advancement in analytical electrochemistry, providing a transferable approach for enhancing sensitivity in biomarker detection with potential applications in clinical diagnostics and biomedical research. The codes and dataset are made publicly available on GitHub to support further research: https://github.com/miralab-ai/biosensors-AI.

1. Introduction

Electrochemical immunosensors represent a powerful analytical platform for biomarker detection, yet achieving ultra-low detection limits remains a fundamental challenge that limits their clinical and diagnostic applications. Traditional electrochemical data analysis approaches face significant limitations that compromise their reliability and sensitivity. Conventional methods, which rely on plotting current versus voltage and selecting peak values, are highly sensitive to baseline drift and electrical noise. This sensitivity can obscure true signals at low analyte concentrations, thereby compromising reliability (Kim and Park, 2021; Xia et al., 2024). Consequently, the limit of detection (LOD) is often constrained by the signal-to-noise ratio, while the linear working range is limited by the sensor's intrinsic transduction mechanism and surface chemistry (Piro and Reisberg, 2017). Furthermore, while performing multiple measurements at the same concentration is a standard procedure to select a reliable value, this approach does not fully mitigate the variability introduced by environmental and instrumental factors, thus hampering overall reproducibility (Mollarasouli et al., 2019). The classical differential pulse voltammetry (DPV) approach focuses on peak current values to construct calibration curves and calculate LOD from blank signal standard deviation. While effective for moderate concentrations, this single-point analysis underutilizes the electrochemical response curve, missing valuable information that could enhance detection sensitivity (Armbruster and Pry, 2008).

☆ This article is part of a Special issue entitled: 'Smart Biosensors' published in Biosensors and Bioelectronics: X.

* Corresponding authors.
E-mail addresses: abdurrahmangumus@isparta.edu.tr (A. Gumus), dilek.odaci.demirkol@ege.edu.tr (D. Odaci).

https://doi.org/10.1016/j.biosx.2025.100733
Received 29 July 2025; Received in revised form 5 November 2025; Accepted 24 December 2025
Available online 5 January 2026

Recent studies have demonstrated the potential of machine learning (ML)-based frameworks in electrochemical sensing, yet their application reveals critical limitations in both methodology and scope, which our study directly addresses. A significant portion of prior work utilizes ML to enhance analysis strictly within the sensor's classical working range, without venturing below the conventional LOD. For instance, the quantitative models developed by Kammarchedu et al. while using multiple ML algorithms like SVM and k-NN, rely on a set of pre-extracted features from the DPV curve, such as peak height, width, and area, rather than the raw data itself (Kammarchedu et al., 2022). Similarly, Liu et al. employ an SVM model fed with the peak currents of different heavy metals, and Zhang et al. use a Back Propagation (BP) neural network that also operates on the peak current values from DPV measurements (Liu et al., 2022; Zhang et al., 2024). These feature-centric approaches, while effective for signals with well-defined peaks, inherently discard the subtle information contained in the rest of the curve and are not designed to function in the noise-dominated region below the classical LOD. Furthermore, the analytical challenge in many of these studies is fundamentally different. Works like Aliev et al. and Liu et al. focus on distinguishing between chemically distinct analytes (e.g., different antibiotics or different heavy metals), where the electrochemical signatures are inherently more dissimilar and thus easier to classify. Even when the full electrochemical spectrum is used, as in the work by Aliev et al. the primary goal is often qualitative classification (presence/absence of an analyte), a trend also highlighted in the review by Aliev et al. (2023), Teng et al. (2023). This is a less demanding task than the one we undertake: differentiating between minute concentration variations of the exact same analyte, where the changes in the DPV curve are far more subtle and complex. Our work, therefore, presents a paradigm shift on multiple fronts: we have developed a quantitative regression framework that not only utilizes the entire DPV curve to capture these subtle signatures but, most critically, demonstrates the ability to provide reliable quantification at ultra-low concentrations that fall below the classical LOD, a domain where previous methods are rendered ineffective.

To address these fundamental limitations, we developed a comprehensive ML-based regression framework for electrochemical immunosensing that shifts the analytical paradigm from single-point peak analysis to complete data-driven analysis. Our approach utilizes the entire DPV curve as information-rich time series data, extracting multiple features and patterns from the complete electrochemical response rather than relying solely on peak current values. This methodology enables more robust and accurate concentration quantification across wide dynamic ranges, establishing a new analytical framework that operates effectively even at ultra-low concentrations where traditional single-point methods become unreliable. By treating electrochemical signatures as comprehensive datasets, our ML-based framework can capture the complete analyte-antibody interaction profile, significantly enhancing detection sensitivity and reliability. To demonstrate the universal applicability of this approach, CD36 was selected as a model analyte for validation and optimization of the proposed analytical framework.

CD36, a membrane protein, plays a crucial role in various physiological and pathological processes, making it a significant target in biomedical research. Its functions encompass lipid metabolism, immune response modulation, and angiogenesis (Silverstein and Febbraio, 2009; Pepino et al., 2014). In lipid metabolism, CD36 facilitates fatty acid uptake in adipose and muscle tissues, thereby regulating energy homeostasis (Glatz et al., 2022). Within the immune system, CD36 aids in pathogen recognition and phagocytosis by immune cells such as macrophages and dendritic cells, thus enhancing the body's defense mechanisms against infections (Baranova et al., 2008). Moreover, CD36's involvement in angiogenesis implicates it in tumor growth and metastasis, as it contributes to the formation of new blood vessels that supply nutrients to growing tumors (Liao et al., 2022). The clinical relevance of CD36 detection is further emphasized by its diagnostic concentrations in biosamples, where soluble CD36 (sCD36) levels are significantly elevated in Type-1 diabetes mellitus patients (42.5 ng/mL) compared to Type-2 diabetes patients (26.1 ng/mL) and non-diabetic individuals (25.3 ng/mL) (Chmielewski et al., 2010), highlighting the need for sensitive detection methods capable of accurately quantifying CD36 across this clinically relevant concentration range.

Current CD36 detection methods face significant limitations across all approaches. Conventional techniques such as immunofluorescence and Western blot suffer from lengthy procedures and limited sensitivity (Miao et al., 2001; Ladányi et al., 2018). While flow cytometry and mass spectrometry offer powerful alternatives (Dzik et al., 2009; Poon et al., 2020), they lack portability and require expensive instrumentation, limiting their applicability in point-of-care settings. Electrochemical immunosensors provide rapid, sensitive, and portable detection, making them particularly beneficial for swift and on-site analysis (Bahadır and Sezgintürk, 2015). These sensors function by detecting binding events between CD36 and Anti-CD36 through measurable electrical signals, typically involving immobilizing Anti-CD36 on an electrode surface. Techniques including cyclic voltammetry (CV), differential pulse voltammetry (DPV), and electrochemical impedance spectroscopy (EIS) are commonly utilized to discern the electrochemical responses elicited by antibody-antigen interactions (Kumar and Kalkal, 2021). However, previous electrochemical approaches for CD36 detection involved complex preparation steps using CNT-modified nanofibers and modified graphene oxide (Er and Odaci Demirkol, 2022; Zeybekler and Odaci, 2023). These approaches required lengthy, multi-step surface modifications with amino group functionalization, resulting in costly procedures, lower sensitivity, and limited linear detection ranges compared to current requirements for clinical applications.

In this study, an electrochemical immunosensor was prepared using polydopamine (PDA)-coated screen-printed electrodes modified with Anti-CD36. The immunosensor was prepared by electropolymerizing PDA on screen-printed electrodes, followed by the conjugation of Anti-CD36. Optimization of the cycle number of PDA and the antibody amount was performed, and the linear range and LOD for CD36 detection were determined using the classical DPV method. PDA electropolymerization enables single-step surface modification, significantly simplifying preparation compared to previous multi-step approaches while improving sensitivity and linear detection range.

Our key contributions include: We developed a comprehensive ML-based regression framework that utilizes the entire DPV curve rather than single peak values, enabling more robust analysis of electrochemical responses. This approach captures the complete electrochemical signature of CD36-antibody interactions across various concentrations, establishing a new quantitative framework that operates effectively across the entire concentration range, including ultra-low concentrations that fall below the classical LOD threshold where traditional methods lose reliability.

We implemented innovative framing techniques and data augmentation strategies specifically designed for electrochemical data, enhancing the robustness and reliability of the analysis while maximizing information extraction from limited experimental datasets. The study presents an optimized PDA-based electrochemical immunosensor with carefully calibrated parameters for electrode modification and antibody conjugation, providing a reliable platform for protein biomarker detection. Most importantly, the developed ML-based framework offers a transferable methodology that can be applied to other electrochemical sensing applications, potentially revolutionizing analytical approaches across various biomedical and environmental monitoring fields.

This ML-based framework represents a paradigm shift in analytical methodology, offering new possibilities for ultrasensitive detection of biomarkers relevant to various diseases and conditions. The significance of this work extends beyond CD36 detection, establishing a foundation for next-generation analytical approaches that can address the growing demand for sensitive, accurate, and reliable biomarker detection in clinical diagnostics and biomedical research.

2. Materials and methods

2.1. Chemicals and reagents

CD36 Monoclonal Antibody (Anti-CD36, 185-1G2, 0.2 mg/mL) was purchased from Thermo Fisher. Recombinant Human CD36 protein (ab167735) was purchased from Abcam. Dopamine (DA; 99.0%) was obtained from Novus Biologicals. N-(3-dimethylaminopropyl)-N'-ethylcarbodiimide hydrochloride (EDC), D-glucose (GLC, 99.5%), urea (99.0–100.5%), insulin (INS), bovine serum albumin (BSA, 98.0%), sodium chloride (NaCl), potassium chloride (KCl), potassium hexacyanoferrate (III) (HCF) (MA 329.24 g/mol, $K_3Fe(CN)_6$), and human serum (H4522) were purchased from Sigma-Aldrich. Pure water used in the experiments was obtained with the Millipore Milli-Q Ultrapure water device.

2.2. Instrumentations

Screen-printed carbon electrodes (SPCE) (Ag/AgCl reference electrode) were purchased from Metrohm (Switzerland). Electrochemical measurements and characterization of immunosensors (CV, DPV, and EIS) were performed using a PalmSens4 potentiostat (Palm Instruments Houten, Netherlands).

2.3. Preparation of PDA/Anti-CD36 immunosensors and electrochemical measurement

PDA film was synthesized via the CV technique. A 1 mg/mL DA solution was prepared in TBS buffer (pH 7.4, 25 mM Tris, 140 mM HCl, 3 mM KCl). By CV technique (potential range between −0.5 V and 0.5 V; scan rate of 20 mV/s), electrochemical deposition of PDA was performed at 5 cycles (Wang et al., 2014). Then, 0.5% (wt%) EDC (in pH 6.0; 50 mM phosphate buffer) was first dropped onto the PDA surface and incubated for 15 min. After that, the electrode surfaces were washed with pure water. After the surfaces were dried, 4.5 μL of 10 μg/mL Anti-CD36 (in pH 7.4; 50 mM PBS) was dropped on PDA-coated surfaces. It was incubated at +4 °C for 24 h. The electrochemical characterization of each modification step in the PDA/Anti-CD36 immunosensor was performed using CV, DPV, and EIS techniques. Measurements were taken after each modification (Bare SPCE, PDA, PDA/Anti-CD36, and PDA/Anti-CD36/CD36). All measurements were conducted in PBS (50 mM PBS, pH 7.4) containing 5 mM hexacyanoferrate (III) ($K_3[Fe(CN)_6]$) and 0.1 M KCl (Karadag et al., 2025; Gelen et al., 2025b,a).

2.4. Optimizing electrochemical data for machine learning via advanced augmentation and preprocessing

The dataset used in this study consists of electrochemical data obtained from CV and DPV measurements for CD36 detection. Measurements were performed across 12 different analyte concentrations. For each concentration, multiple measurements were taken over five measurements, resulting in a comprehensive dataset. As illustrated in Fig. 1, the CV and DPV signals for various analyte concentrations demonstrate the distinct electrochemical behavior of the analytes.

In Machine Learning (ML) applications, the size and quality of the dataset are critical for effective model training. Larger datasets enable ML models to discern complex patterns and relationships within the data, leading to improved performance. However, acquiring large experimental datasets can be challenging due to economic and time constraints. Data augmentation techniques have been extensively applied to address these challenges by artificially expanding datasets, introducing diversity, and improving the generalization capabilities of ML models (Wang et al., 2024; Wen et al., 2021). To overcome this limitation, we generated additional signals by applying a convex combination to pairs of existing measurements, in line with the pairwise data augmentation approach (Zhang et al., 2017). Specifically, for each unique pair of measurements, a new signal was created according to the following formula:

$$Signal_{\text{new}} = (1-\alpha)\, Signal_1 + \alpha\, Signal_2 \tag{1}$$

where α is a weighting coefficient in the range $[0, 1]$. For each class, new signals were generated for all 10 unique measurement pairs, resulting in 50 additional signals per class. These synthetic signals were then combined with the original dataset to enhance both the size and diversity of the training data. The interpolation process used to generate these signals is illustrated in Fig. 1. By focusing on the first five data points of each measurement, we aimed to capture the initial response of the analytes during voltammetric analysis, while minimizing variations arising from factors such as electrode condition and analyte diffusion kinetics.

Advanced signal processing techniques have been shown to improve the extraction of high-quality features from electrochemical signals, enabling more reliable analysis and better model performance (Li et al., 2024). Careful selection of signal processing methods is critical to avoid distortions and ensure the reliability of the extracted features, particularly when analyzing sensitive regions (Jakubowska, 2011). In this context, we employed windowing, a fundamental and widely adopted technique in signal processing and machine learning for analyzing time-series data (Géron, 2022; Goodfellow et al., 2016). This approach systematically extracts localized features by segmenting a signal into smaller parts and is considered a standard practice in diverse fields, from human activity recognition (Saeed et al., 2019) and time-series classification (Fawaz et al., 2018) to its implementation in modern ML software libraries (Löning et al., 2019). In this study, framing techniques were applied exclusively to DPV signals due to their higher sensitivity to analyte concentration and the presence of well-defined peak regions. This process involved segmenting the DPV curves into windows of varying sizes, allowing the extraction of localized features from different regions of the signal.

The selected regions for windowing were chosen to focus on areas near the peak regions of the DPV signals, as these regions are most sensitive to changes in analyte concentration. Starting from the peak region, the window size was gradually increased to capture both localized and broader signal characteristics, ensuring that critical information near the peak was preserved while incorporating the overall signal behavior for a more comprehensive analysis. As illustrated in Fig. 2, the DPV measurements were analyzed both without windowing (top left) and with varying window lengths across different sample index ranges. The windowing process was performed for sample indices ranging from 100 to 120, 90 to 130, 80 to 140, 70 to 150, and 60 to 160, with each window capturing distinct signal characteristics. These regions were selected based on their proximity to the peak regions, which are critical for accurate regression model predictions.

2.5. Machine learning framework

The electrochemical data were subjected to a systematic preprocessing framework to prepare them for the regression models. Initially, a windowing technique was applied to extract features from different time intervals of the DPV curve, with a separate regression analysis performed for each window. The sizes of these windows, which determine the input data dimension for the regression model, ranged from 20 to 100 data points. In contrast to traditional univariate analysis, this approach enabled the investigation of different regions of the DPV curve via multivariate regression analysis in a high-dimensional data space.

Subsequently, the dataset obtained from each window was partitioned into 80% training and 20% testing subsets. During this partitioning, a stratified random splitting method was employed to preserve the proportional distribution of each concentration level in both the

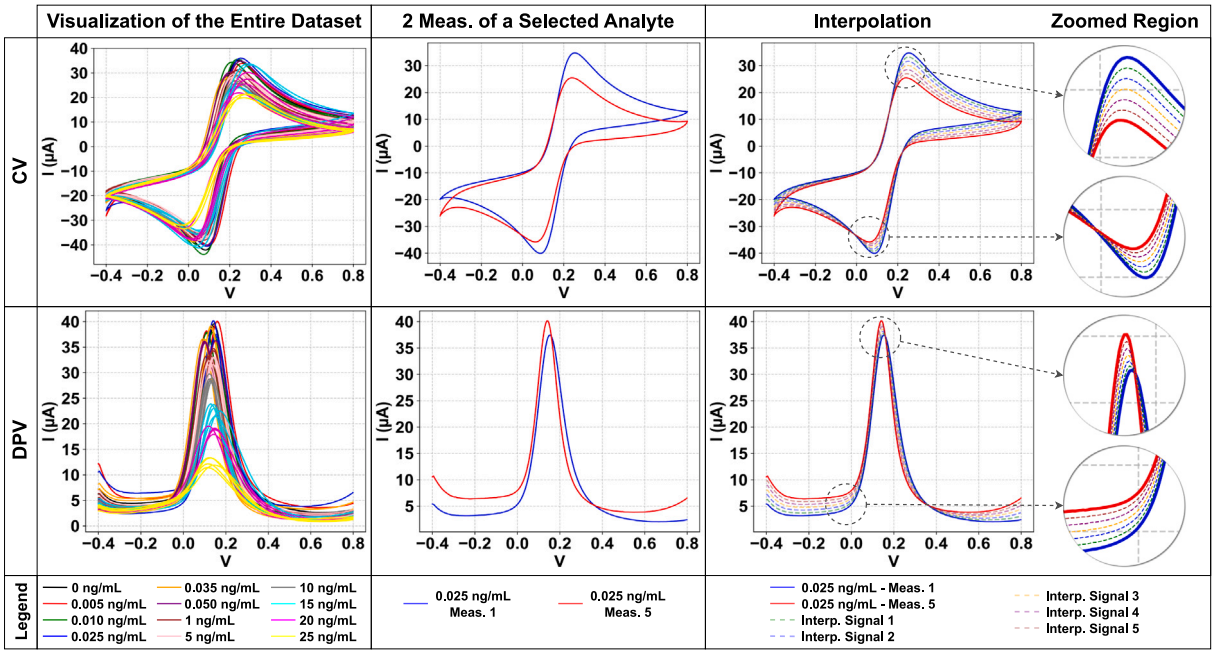

Fig. 1. Interpolation process for augmenting an electrochemical dataset. The top row displays cyclic voltammetry (CV) data, and the bottom row shows differential pulse voltammetry (DPV) data. (a, d) Visualization of the entire experimental dataset containing various analyte concentrations. (b, e) Two distinct measurements (Measurement 1 and Measurement 5) from the 0.025 ng analyte measurement are isolated to serve as boundary signals. (c, f) Application of a convex combination method to generate five new, evenly spaced synthetic signals between the two real measurements, effectively increasing the dataset's density. The magnified insets confirm the smooth and progressive nature of the interpolated curves.

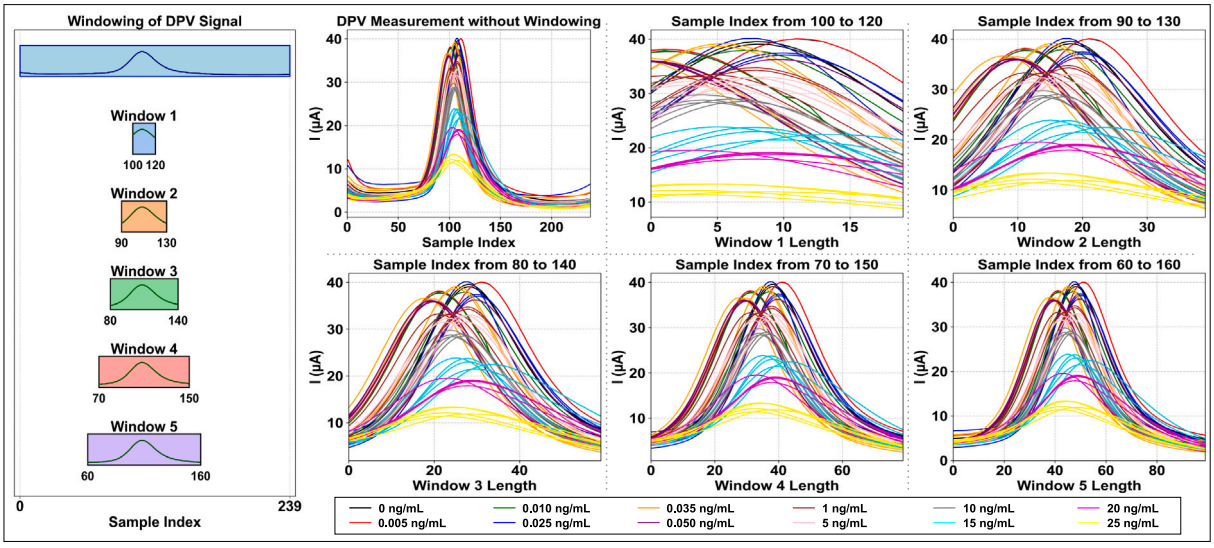

Fig. 2. Application of the windowing technique for feature extraction from DPV signals. This data preprocessing step segments the DPV curves into five windows of varying sizes centered around the signal peak to capture critical information for the machine learning models. The full signal (top center) is compared with five specific windows: Window 1 (100–120), Window 2 (90–130), Window 3 (80–140), Window 4 (70–150), and Window 5 (60–160), a process that provides the machine learning models with multi-scale features from the most information-rich area of the signal.

training and testing sets. To prevent data leakage and optimize model performance, a feature scaling process was implemented. In this step, a standard scaler was trained using only the training data, and the learned transformation parameters (mean and standard deviation) were applied to both the training and test data. This procedure standardized each feature to a mean of zero and a standard deviation of one, thereby preventing variables at different scales from adversely affecting model performance.

In this study, various regression models were employed to evaluate the predictive performance of the prepared electrochemical data. The selection of a diverse set of models aimed to identify which model performs optimally under different data structures and characteristics inherent to electrochemical measurements. Table 1 summarizes the regression models used in this study, highlighting their core principles, advantages, and example applications.

Each model offers distinct advantages and limitations, making them suitable for different aspects of electrochemical data analysis. The performance of these models was evaluated using standard regression metrics, such as the coefficient of determination (R^2), Root Mean Squared Error (RMSE), and Mean Absolute Error (MAE), to determine

Table 1
Summary of regression models used in this study. Abbreviations: LR—Linear Regression, SVR—Support Vector Regression, DT—Decision Tree, RF—Random Forest, GBR—Gradient Boosting Regressor, GPR—Gaussian Process Regressor, KNN—K-Nearest Neighbors, MLP—Multi-Layer Perceptron, 1D-CNN—One-Dimensional Convolutional Neural Network. Each model is characterized by its core principle, key advantages & disadvantages, and applications across different domains.

Abbr.	Core principle	Advantages & Disadvantages	Applications
LR	Assumes linear relationship between variables, minimizing sum of squared residuals using ordinary least squares method (Roustaei, 2024).	Simple and interpretable but struggles with outliers and non-linear relationships.	(Luo and Qi, 2017) (Oishi et al., 2020) (Sun et al., 2021)
SVR	Fits a hyperplane within an epsilon-insensitive tube using kernel functions (Valkenborg et al., 2023).	Handles non-linearity and high-dimensional data but is computationally intensive and hyperparameter sensitive.	(Lu et al., 2009) (Suganyadevi and Babulal, 2014) (Valente and Maldonado, 2020)
DT	Predicts outcomes by recursively splitting data based on feature values (Vanneschi and Silva, 2023).	Interpretable and captures non-linearity but prone to overfitting.	(Henderson et al., 2005) (Benkercha and Moulahoum, 2018) (Elmachtoub et al., 2020)
RF	Combines multiple decision trees, trained on random subsets of data and features (Iranzad and Liu, 2025).	Provides high accuracy and reduces overfitting but less interpretable and memory intensive.	(Wang et al., 2018) (Chencho et al., 2020) (Anjum et al., 2022)
GBR	Builds a series of weak learners sequentially, correcting residuals of the previous one (Bentéjac et al., 2021).	Achieves high accuracy and captures complex patterns but computationally intensive and hyperparameter sensitive.	(Agapitos et al., 2017) (Sapountzoglou et al., 2020) (Di Persio and Fraccarolo, 2023)
GPR	A probabilistic method based on Bayesian principles, modeling data as a distribution over functions (Marrel and Iooss, 2024).	Quantifies uncertainty and models non-linearity but has $O(n^3)$ complexity and kernel sensitivity.	(Wistuba et al., 2017) (Zhou and Peng, 2020) (Born and Kästner, 2021)
KNN	Predicts based on average of k nearest neighbors using distance metric (Halder et al., 2024).	Flexible with no distribution assumptions but computationally expensive and sensitive to noise.	(Zhou et al., 2016) (Gou et al., 2019) (Martínez et al., 2019)
MLP	A neural network modeling complex, non-linear relationships using multiple layers (Hoya, 2024).	Effective for high-dimensional and complex data but computationally intensive and prone to overfitting.	(Kosicka et al., 2022) (Sumorek and Idzkowski, 2023) (Setiawan et al., 2024)
1D-CNN	Designed for one-dimensional data like time series, extracting local patterns via convolutional layers (Ige and Sibiya, 2024).	Extracts local features and ideal for time series but computationally intensive and needs sufficient data.	(Liu and Si, 2022) (Kim et al., 2023) (Aljafari et al., 2024)

the most effective approach for predicting analyte concentrations from the processed electrochemical signals.

3. Results and discussion

3.1. Characterization and application of PDA/Anti-CD36 immunosensor

The stepwise fabrication process of the PDA/Anti-CD36/CD36 immunosensor is shown in Fig. 3.a. PDA used as the immobilization matrix was obtained by depositing DA on the SPCE surface using the CV technique. To determine the optimal number of cycles, DA was deposited onto the SPCE surface for 5, 10, and 20 cycles. The modified surfaces were characterized using CV, DPV, and EIS techniques, and the corresponding profiles are presented in Figure S1.a (CV), Figure S1.b (DPV), and Figure S1.c (EIS). The results show that there is not much difference between 5 and 10 cycles, but the current decreases significantly at 20 cycles. Based on the results, 5 cycles were selected

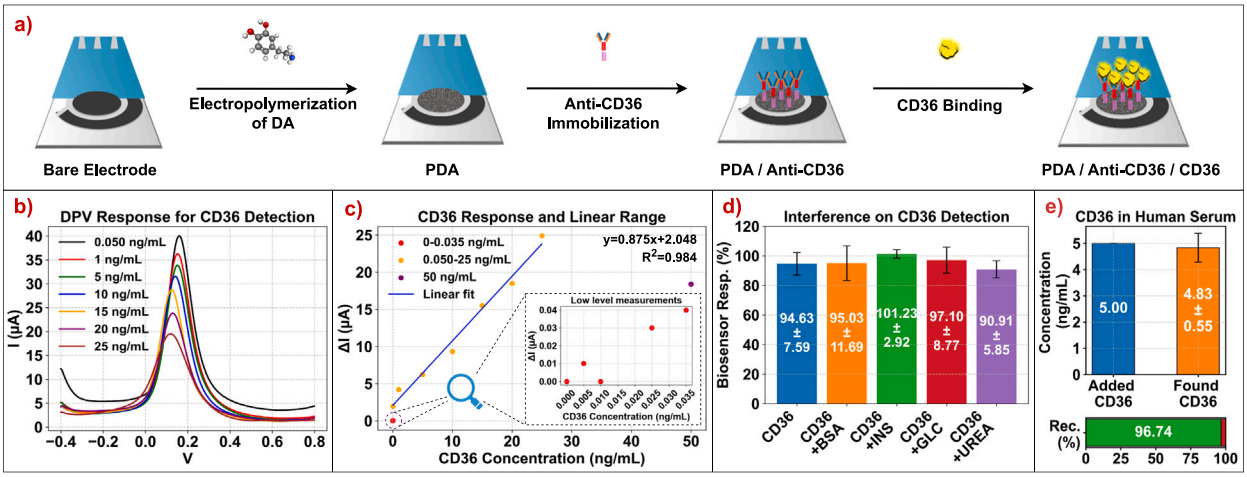

Fig. 3. (a) Schematic representation of the preparation of PDA/Anti-CD36/CD36 immunosensor, (b) DPV profile corresponding to increasing CD36 concentration between 0.05 and 25 ng/mL, (c) Linear detection range for CD36 using the SPCE/PDA/Anti-CD36 immunosensor, (d) Effect of some interfering compounds to signal of SPCE/PDA/Anti-CD36 to CD36, ([CD36]: 10 ng/mL, [BSA]; 4 g/dL, [INS]: 10 µU/mL; [GLC]; 100 mg/dL, [Urea]: 14 mg/dL), (e) results of the sample application.

for further experiments. Figure S1.d shows the cyclic voltammogram of PDA deposition by electropolymerization of DA over 5 cycles.

As seen in Figure S1.d, an anodic peak was observed at 0.21 V and two cathodic peaks at −0.12 V and −0.14 V. The observed voltammetric responses can be attributed to dopamine/dopaminequinone and leucodopaminchrome /dopaminechrome redox couples (Li et al., 2006). This suggests that an electrochemically inactive insulating PDA coating is formed at the electrode–solution interface, preventing the electrochemical oxidation of DA. Optimization of the Anti-CD36 concentration was performed using the DPV method. Antibody concentrations of 5, 10, and 20 µg/mL were immobilized on the SPCE/PDA surface. Current changes corresponding to different Anti-CD36 concentrations are shown in Figure S1.f. The highest binding was found at 10 µg/mL Anti-CD36 concentration. The optimum Anti-CD36 concentration was determined as 10 µg/mL. The SEM image of the SPCE/PDA surface is shown in Figure S1.e.

Electrochemical characterization of the PDA/Anti-CD36 surface was performed using CV, DPV, and EIS measurements. Electrochemical oxidation and reduction peaks of potassium hexacyanoferrate (HCF) were examined in the CV profiles of each modification step of the prepared immunosensor surface. According to the CV voltammograms (Figure S1.g), the ianodic values were found to be 62.99 µA, 48.41 µA, 35.52 µA, and 27.46 µA for SPCE, PDA, PDA/Anti-CD36, and PDA/Anti-CD36/CD36, respectively. A significant decrease was observed in the currents obtained after each modification step for bare SPCE containing PDA, PDA/Anti-CD36, and PDA/Anti-CD36/CD36. This supports the success of all modifications.

In the DPV profile (Figure S1.h), the current values after each modification were found to be 47.59 µA, 21.43 µA, 16.71 µA, and 9.15 µA for SPCE, PDA, PDA/Anti-CD36, and PDA/Anti-CD36/CD36, respectively. A significant decrease was observed in the voltammograms obtained after each modification step for SPCE, PDA/Anti-CD36, and PDA/Anti-CD36/CD36.

Finally, the EIS technique (Figure S1.i) was used to determine how the resistances of the prepared surfaces changed after each modification. In EIS, the diameter of the semicircle is proportional to the increase in charge transfer resistance. The increase in the diameter of the semicircle indicates the formation of an insulating layer on the surfaces and a decrease in electron transfer. The EIS diagrams of the SPCE, PDA, PDA/Anti-CD36, and PDA/Anti-CD36/CD36 surfaces show that the surface resistance increases and the semicircle enlarges after each modification. This supports the results obtained from the CV and DPV techniques.

The DPV profile corresponding to increasing CD36 concentrations from 0.05 to 25 ng/mL is given in Fig. 3.b. To determine the linear detection range of the PDA/Anti-CD36 immunosensor, DPV measurements were performed in 10 different CD36 concentration ranges between 0.05–50 ng/mL. The linear range of the developed PDA/Anti-CD36 immunosensor was determined as 0.05–25 ng/mL, and the calibration equation was $y = 0.875x + 2.048$ and $R^2 = 0.984$. In addition, no current difference could be determined electrochemically at concentrations lower than 0.05 ng/mL (Fig. 3.c). To calculate the LOD of the PDA/Anti-CD36 immunosensor, 7 different DPV measurements were made with a CD36 concentration of 0.05 ng/mL, which was the lowest point of the calibration curve. SD and LOD were calculated using the formula 3SD/m (SD: standard deviation of 7 measurements performed at the lowest point of the calibration curve and m: slope of the calibration curve). The LOD of PDA/Anti-CD36 was calculated as 0.034 ng/mL CD36.

To investigate the specificity of PDA/Anti-CD36 for CD36, electrochemical measurements were performed in the presence of some potentially interfering compounds such as BSA, GLC, INS, and UREA. The recovery percentages were calculated as 95.35% for CD36+BSA, 101.235% for CD36+INS, 97.1% for CD36+GLC, and 95.79% for CD36+UREA. Fig. 3.d shows that PDA/Anti-CD36 has good selectivity for CD36 and that these compounds do not cause interference. To evaluate the CD36 detection performance of PDA/Anti-CD36 in real samples, a known concentration of CD36 was added to commercial human serum. The recovery percentage of CD36 was found to be 96.74% (Fig. 3.e).

3.2. Machine learning framework performance analysis for analytical detection of CD36

The performance of the machine learning framework for the analytical detection of CD36 was systematically evaluated. This evaluation focused on the impact of two key strategies: the application of data augmentation and the expansion of the DPV signal region used for analysis. The models' predictive capabilities were rigorously assessed using both quantitative performance metrics, summarized in Table 2, and a detailed visual analysis of their predictive behavior and error patterns, presented in Fig. 4. The following analysis demonstrates that the combination of these strategies not only improves overall accuracy but also significantly extends the sensor's effective quantification range to levels below the conventional LOD.

Table 2
Regression model performance metrics for CD36 detection. Models were evaluated across different data region ranges and augmentation conditions. Broader data regions and the application of data augmentation improved the performance, particularly for Gradient Boosting and Random Forest.

Aug.	Model Name	Single point			100–120			90–130			80–140			70–150			60–160		
		R2	*RMSE*	*MAE*	*R2*	*RMSE*	*MAE*	*R2*	*RMSE*	*MAE*	*R2*	*RMSE*	*MAE*	*R2*	*RMSE*	*MAE*	*R2*	*RMSE*	*MAE*
No Augmentation	Linear Regression	0.85	1.34	1.23	0.9	1.08	0.94	−0.3	3.9	2.19	0.69	1.92	1.21	0.79	1.58	0.95	0.82	1.47	0.91
	SVR	0.93	0.92	0.66	0.85	1.33	0.93	0.88	1.21	0.87	0.89	1.17	0.88	0.9	1.09	0.89	0.89	1.15	0.97
	Decision Tree	0.88	1.19	0.42	0.99	0.41	0.17	0.99	0.41	0.17	0.99	0.29	0.08	0.99	0.41	0.17	0.99	0.41	0.17
	Random Forest	0.89	1.17	0.47	0.98	0.43	0.27	0.99	0.42	0.3	0.99	0.4	0.28	0.98	0.43	0.29	0.99	0.42	0.3
	Gradient Boosting	0.88	1.19	0.42	0.99	0.39	0.18	0.99	0.39	0.17	0.99	0.41	0.19	0.99	0.34	0.16	0.99	0.35	0.16
	Gaussian P. Regressor	0.89	1.13	0.59	0.96	0.69	0.44	0.69	1.93	1.31	0.13	3.21	2.14	−0.7	4.44	2.95	−1.4	5.32	3.88
	K-Nearest Neighbors	0.92	1	0.58	0.96	0.65	0.5	0.97	0.62	0.47	0.97	0.59	0.43	0.97	0.62	0.5	0.93	0.89	0.8
	MLP Regression	0.94	0.84	0.53	0.57	2.27	1.96	0.77	1.66	1.39	0.8	1.55	1.33	0.85	1.33	1.19	0.82	1.47	1.24
	1D-CNN	−1.1	4.97	4.14	−0.5	4.24	3.44	−0.6	4.36	3.56	−0.6	4.32	3.56	−1.1	5.01	4.17	−0.9	4.74	3.86
Augmentation Applied	Linear Regression	0.83	1.42	1.19	0.96	0.65	0.55	0.99	0.29	0.22	1	0.1	0.03	1	0.1	0.03	1	0.1	0.03
	SVR	0.93	0.88	0.53	0.98	0.51	0.3	0.99	0.31	0.22	0.99	0.31	0.22	0.99	0.28	0.2	0.99	0.27	0.19
	Decision Tree	0.97	0.57	0.19	1	0.23	0.05	1	0.23	0.04	1	0.19	0.04	1	0.17	0.03	1	0.15	0.02
	Random Forest	0.97	0.55	0.25	1	0.2	0.07	1	0.14	0.05	1	0.14	0.05	1	0.13	0.05	1	0.12	0.05
	Gradient Boosting	0.98	0.52	0.3	1	0.17	0.09	1	0.13	0.07	1	0.13	0.07	1	0.15	0.09	1	0.17	0.09
	Gaussian P. Regressor	0.94	0.86	0.54	1	0.11	0.03	1	0.14	0.05	0.99	0.3	0.1	0.98	0.55	0.23	0.93	0.94	0.4
	K-Nearest Neighbors	0.96	0.66	0.33	1	0.22	0.1	1	0.22	0.09	1	0.22	0.1	1	0.18	0.08	0.99	0.3	0.12
	MLP Regression	0.94	0.87	0.59	0.98	0.53	0.44	0.97	0.64	0.49	0.95	0.79	0.58	0.96	0.73	0.54	0.97	0.63	0.47
	1D-CNN	0.89	1.12	0.93	0.99	0.34	0.28	0.95	0.74	0.56	0.99	0.31	0.26	0.97	0.59	0.46	0.97	0.63	0.47

The regression analysis presented in Table 2 demonstrates that the accuracy of CD36 concentration prediction is improved by the strategies of data augmentation and the expansion of the analytical signal window. The transformative effect of data augmentation is most prominently observed in the 1D-CNN model; this model, which exhibited a completely unacceptable performance with an R^2 of −1.07 and an RMSE of 4.9669 in the single-point analysis without augmentation, became a statistically significant model by achieving an R^2 of 0.9664 and an RMSE of 0.633 in the 60–160 range when augmentation was applied. This strategy also elevated already competent models like Random Forest to near-perfection; in the 60–160 range, it increased the R^2 value from 0.9854 to 0.9988 while reducing the RMSE from 0.4172 to an extremely low level of 0.122. Secondly, the contribution of expanding the analysis window to performance is also clear. For instance, the augmented Gradient Boosting model improved its performance from an R^2 of 0.9772 and an RMSE of 0.5213 in the single-point analysis to an R^2 of 0.9976 and an RMSE of 0.168 by incorporating the holistic signal features within the 60–160 range. When these two approaches were combined, ensemble algorithms such as Random Forest, Gradient Boosting, and Decision Tree demonstrated outstanding prediction precision, consistently achieving R^2 values above 0.998 and reducing MAE values below 0.05 in wide windows. Another noteworthy finding is that even the Linear Regression model, when supported by data augmentation, could produce best-in-class results with an R^2 of 0.9992 and an MAE of 0.0271 in the 60–160 range, which implies that augmentation simplifies the feature space, making it suitable for linear models. In conclusion, these findings prove that treating the raw signal data as a time series and enriching it with synthetic data overcomes the limitations of traditional electrochemical analysis methods. This approach provides the capability to include even low concentrations in the regression evaluation — concentrations that are typically excluded from regression calculations with conventional methods because they fall below the LOD — and that these are indispensable engineering approaches for developing robust and reliable biosensor systems with high accuracy and repeatability.

Fig. 4 complements these numerical results by qualitatively revealing the behavioral nuances and error patterns of the models. The figure allows for an examination of not only the models' average error metrics but also the distribution, variance, and systematic deviations of their predictions. In this context, the confusion matrix, essentially a classification metric, has been employed as an insightful supplementary tool to diagnose the concentration ranges where the models experience "confusion" by rounding the regression outputs to the nearest concentration level. The regression plots in the upper panels visually expose the fundamental behaviors and weaknesses of the models. For instance, the Linear Regression in the narrow window (Fig. 4.a), in addition to its high RMSE, exhibits a pronounced deviation from the ideal prediction line, showing a tendency to systematically overestimate low concentrations and underestimate high concentrations. This visually confirms the model's inability to capture the non-linear dynamics in the data. In contrast, the predictions of the Gradient Boosting model (Fig. 4.b, Fig. 4.e), with their tightly clustered, narrow box plots around the ideal line, visually confirm its robustness through both high accuracy (low bias) and high precision (low variance). The transformative effect of a wider window on the Linear Regression model (Fig. 4.d) and the stabilization of its prediction curve prove that a broader signal range provides critical discriminative information. The most insightful contribution of the figure is its diagnosis of the nature of regression errors via the confusion matrices in the lower panels. These matrices provide the definitive visual evidence that substantiates one of the study's most important claims: the capability for sub-LOD quantification. The dense, off-diagonal error pattern of the Linear Regression matrix in the narrow window (Fig. 4.a) shows its inability to reliably distinguish between adjacent low concentrations, particularly 0 ng and 0.005 ng. Conversely, the sharply diagonalized matrices of the superior models in the wide window (Fig. 4.d, Fig. 4.e), beyond proving their high discriminative power, reveal a critical fact in their top-left corners: an almost error-free discrimination is achieved between the blank sample (0 ng) and ultra-low concentrations such as 0.005 ng and 0.010 ng. This successful and clear classification at levels indistinguishable from noise by traditional methods concretely supports the finding that the developed framework extends the analytical sensitivity of the sensor beyond classical limits, enabling reliable quantification in a previously unmeasurable range.

4. Conclusion

This study focused on a ML-based approach for low-concentration analysis, developing a PDA-modified immunosensor for CD36 detection and establishing an analytical framework that surpasses the limitations of conventional methods. While the conventional analysis method had a limited range (0.05–25 ng/mL) and $R^2 \approx 0.984$, the proposed ML-based approach enables numerical estimation of the analyte across the entire concentration range, including below LOD, by processing the DPV curve as a time series ($R^2 \approx 0.999$). The obtained findings demonstrate that a paradigmatic shift in electrochemical sensor technology is possible. In contrast to conventional single-point analysis approaches, using the complete electrochemical response as an information source

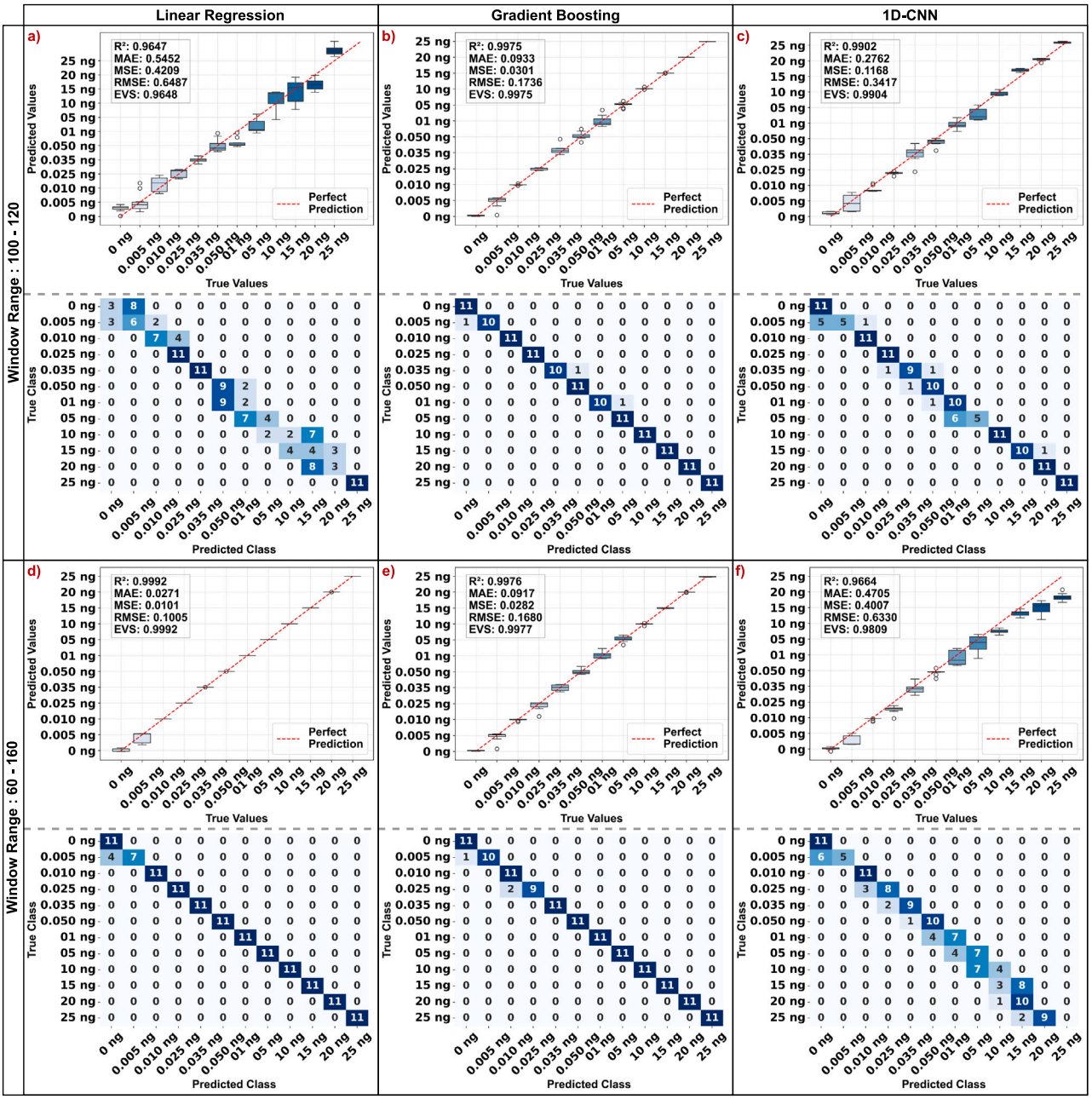

Fig. 4. Comparison of Linear Regression, Gradient Boosting, and 1D-CNN models for CD36 detection using two data windows: (a–c) 100–120 and (d–f) 60–160. Upper panels show predicted vs. true values (red dashed line indicates perfect prediction); lower panels display confusion matrices with diagonal elements representing correct classifications. Off-diagonal elements and deviations from the red line indicate prediction errors, revealing performance differences across models and data ranges. (For interpretation of the references to color in this figure legend, the reader is referred to the web version of this article.)

significantly expands the analytical capacity of sensors. Among the tested models, Random Forest and Gradient Boosting provided the most accurate results, while linear regression also performed strongly after data augmentation. Deep learning models like 1D-CNN required data augmentation to reach comparable performance. The most important contribution of this study is providing reliable quantification at concentration levels previously considered unmeasurable by going beyond the classical LOD concept. This achievement can enhance early diagnosis opportunities in clinical diagnostic applications and enable more sensitive evaluations in disease monitoring processes. Furthermore, the adaptability of the developed methodology to other biomarkers and sensor platforms creates new opportunities for wide-scale applications in the field of electrochemical analysis.

However, comprehensive validation studies are needed to reveal the full potential of this approach. Evaluating performance under different environmental conditions, matrix effects, and sensor-to-sensor variations is critical for the reliable application of the methodology in clinical settings. Future research should aim for the integration of the developed approach into standard analytical protocols by overcoming these limitations. In conclusion, this study makes a significant methodological contribution to the electrochemical analysis literature by redefining the analytical limits of sensor technology and represents an important step toward developing more sensitive, reliable, and accessible diagnostic tools in biomedical applications. This approach has the potential to revolutionize personalized medicine and point-of-care applications in the future.

CRediT authorship contribution statement

Muhammet Cagri Yeke: Writing – original draft, Visualization, Validation, Software, Methodology, Investigation, Formal analysis, Data curation, Conceptualization. **Sultan Sacide Gelen:** Writing – original draft, Visualization, Validation, Software, Methodology, Investigation, Formal analysis, Data curation, Conceptualization. **Hilal Fil:** Formal analysis, Data curation. **Muhammet Mustafa Yalcin:** Formal analysis, Data curation. **Abdurrahman Gumus:** Writing – review & editing, Visualization, Validation, Supervision, Software, Resources, Project administration, Methodology, Investigation, Funding acquisition, Formal analysis, Data curation, Conceptualization. **Idris Yazgan:** Writing – review & editing, Supervision. **Dilek Odaci:** Writing – review & editing, Supervision, Project administration, Funding acquisition.

Declaration of Generative AI and AI-assisted technologies in the writing process

During the preparation of this work, the author(s) used ChatGPT to enhance the clarity and coherence of the text. After using this tool/service, the author(s) reviewed and edited the content as needed and take full responsibility for the content of the publication.

Declaration of competing interest

The authors declare that they have no known competing financial interests or personal relationships that could have appeared to influence the work reported in this paper.

Acknowledgments

The authors would like to express their gratitude to the *Machine Intelligence Research and Applications Laboratory* and the *Nanobiotechnology Research Lab.* at Izmir Institute of Technology and Ege University for their valuable support throughout this study.

Appendix A. Supplementary data

Supplementary material related to this article can be found online at https://doi.org/10.1016/j.biosx.2025.100733.

Data availability

The dataset generated and analyzed during the current study, along with the corresponding source code, are openly available in a public GitHub repository. The dataset was created at the *Nanobiotechnology Research Laboratory*, Department of Biochemistry, Ege University. The resources can be accessed at the following address: https://github.com/miralab-ai/biosensors-AI.

References

Agapitos, A., Brabazon, A., O'Neill, M., 2017. Regularised gradient boosting for financial time-series modelling. Comput. Manag. Sci. 14, 367–391. http://dx.doi.org/10.1007/s10287-017-0280-y.

Aliev, T.A., Belyaev, V.E., Pomytkina, A.V., Nesterov, P., Shityakov, S., Sadovnichii, R.V., Novikov, A.S., Orlova, O., Masalovich, M.S., Skorb, E., 2023. Electrochemical sensor to detect antibiotics in milk based on machine learning algorithms. ACS Appl. Mater. & Interfaces http://dx.doi.org/10.1021/acsami.3c12050.

Aljafari, B., Satpathy, P.R., Thanikanti, S.B., Nwulu, N., 2024. Supervised classification and fault detection in grid-connected PV systems using 1D-CNN: Simulation and real-time validation. Energy Rep. 12, 2156–2178. http://dx.doi.org/10.1016/j.egyr.2024.08.008, URL https://www.sciencedirect.com/science/article/pii/S2352484724004992.

Anjum, M.N., Khan, K., Ahmad, W., Ahmad, A., Amin, M., Nafees, A., 2022. Application of ensemble machine learning methods to estimate the compressive strength of fiber-reinforced nano-silica modified concrete. Polymers 14, http://dx.doi.org/10.3390/polym14183906.

Armbruster, D., Pry, T., 2008. Limit of blank, limit of detection and limit of quantitation. Clin. Biochem. Rev. 29 Suppl 1, S49–52, URL https://www.ncbi.nlm.nih.gov/pmc/articles/PMC2556583/.

Bahadır, E., Sezgintürk, M., 2015. Applications of electrochemical immunosensors for early clinical diagnostics. Talanta 132, 162–174. http://dx.doi.org/10.1016/J.TALANTA.2014.08.063.

Baranova, I., Kurlander, R., Bocharov, A., Vishnyakova, T., Chen, Z., Remaley, A., Csako, G., Patterson, A., Eggerman, T., 2008. Role of human CD36 in bacterial recognition, phagocytosis, and pathogen-induced JNK-mediated Signaling1. J. Immunol. 181, 7147–7156. http://dx.doi.org/10.4049/jimmunol.181.10.7147.

Benkercha, R., Moulahoum, S., 2018. Fault detection and diagnosis based on C4.5 decision tree algorithm for grid connected PV system. Sol. Energy http://dx.doi.org/10.1016/J.SOLENER.2018.07.089.

Bentéjac, C., Csörgő, A., Martínez-Muñoz, G., 2021. A comparative analysis of gradient boosting algorithms. Artif. Intell. Rev. 54 (3), 1937–1967. http://dx.doi.org/10.1007/s10462-020-09896-5.

Born, D., Kästner, J., 2021. Geometry optimization in internal coordinates based on Gaussian process regression: Comparison of two approaches. J. Chem. Theory Comput. http://dx.doi.org/10.1021/acs.jctc.1c00517.

Chencho, Li, J., Hao, H., Wang, R., Li, L., 2020. Development and application of random forest technique for element level structural damage quantification. Struct. Control. Health Monit. 28, http://dx.doi.org/10.1002/stc.2678.

Chmielewski, M., Bragfors-Helin, A.-C., Stenvinkel, P., Lindholm, B., Anderstam, B., 2010. Serum soluble CD36, assessed by a novel monoclonal antibody-based sandwich ELISA, predicts cardiovascular mortality in dialysis patients. Clin. Chim. Acta 411 (23), 2079–2082. http://dx.doi.org/10.1016/j.cca.2010.09.009, URL https://www.sciencedirect.com/science/article/pii/S0009898110005759.

Di Persio, L., Fraccarolo, N., 2023. Energy consumption forecasts by gradient boosting regression trees. Mathematics http://dx.doi.org/10.3390/math11051068.

Dzik, W., Cserti-Gazdewich, C., Ssewanyana, I., Delelys, M., Preffer, F., 2009. When monocytes and platelets compete: The effect of platelet count on the flow cytometric measurement of monocyte CD36. Cytom. Part B: Clin. Cytom. 78B, http://dx.doi.org/10.1002/cyto.b.20504.

Elmachtoub, A.N., Liang, J.C.N., McNellis, R., 2020. Decision trees for decision-making under the predict-then-optimize framework. pp. 2858–2867. http://dx.doi.org/10.48550/arXiv.2003.00360, arXiv e-prints.

Er, S., Odaci Demirkol, D., 2022. Graphene oxide incorporated polystyrene electrospun nanofibers for immunosensing of CD36 as a marker of diabetic plasma. Bioelectrochemistry 145, 108083. http://dx.doi.org/10.1016/j.bioelechem.2022.108083, URL https://www.sciencedirect.com/science/article/pii/S1567539422000342.

Fawaz, H.I., Forestier, G., Weber, J., Idoumghar, L., Muller, P.-A., 2018. Deep learning for time series classification: a review. Data Min. Knowl. Discov. 33, 917–963. http://dx.doi.org/10.1007/s10618-019-00619-1.

Gelen, S.S., Cifci, A., Azak, H., Yalcinkaya, E.E., Zeybekler, S.E., Odaci, D., 2025a. Electropolymerization of organoclays and usage of synthesized polymer-clay nanocomposite as a matrix for cell adhesion. Prog. Org. Coatings 206, 109334. http://dx.doi.org/10.1016/j.porgcoat.2025.109334, URL https://www.sciencedirect.com/science/article/pii/S0300944025002838.

Gelen, S.S., Gokce, B., Yazgan, İ., Saygili, E., Karakuş, H.S., Goksel, T., Odaci, D., 2025b. Immunosensing of C-reactive protein in pleural fluid using electrodeposited silver nanoparticles. Talanta 128931. http://dx.doi.org/10.1016/j.talanta.2025.128931, URL https://www.sciencedirect.com/science/article/pii/S0039914025014225.

Géron, A., 2022. Forecasting time series. In: Hands-on Machine Learning with Scikit-Learn, Keras & TensorFlow, third ed. O'Reilly Media, pp. 499–538, URL https://www.oreilly.com/library/view/hands-on-machine-learning/9781098125967/.

Glatz, J., Nabben, M., Luiken, J., 2022. CD36 (SR-B2) as master regulator of cellular fatty acid homeostasis. Curr. Opin. Lipidol. 33, 103–111. http://dx.doi.org/10.1097/MOL.0000000000000819.

Goodfellow, I., Bengio, Y., Courville, A., 2016. Sequence modeling: Recurrent and recursive nets. In: Deep Learning. MIT Press, pp. 367–416, URL http://www.deeplearningbook.org.

Gou, J., Qiu, W., Yi, Z., jun Shen, X., Zhan, Y., Ou, W., 2019. Locality constrained representation-based K-nearest neighbor classification. Knowl.-Based Syst. 167, 38–52. http://dx.doi.org/10.1016/j.knosys.2019.01.016.

Halder, R.K., Uddin, M.N., Uddin, M.A., Aryal, S., Khraisat, A., 2024. Enhancing K-nearest neighbor algorithm: a comprehensive review and performance analysis of modifications. J. Big Data 11 (1), 113. http://dx.doi.org/10.1186/s40537-024-00973-y.

Henderson, B., Bui, E., Moran, C., Simon, D., 2005. Australia-wide predictions of soil properties using decision trees. Geoderma 124, 383–398. http://dx.doi.org/10.1016/J.GEODERMA.2004.06.007.

Hoya, T., 2024. Review of the two existing artificial neural network models—Multilayer perceptron and probabilistic neural networks. In: Syntactic Networks—Kernel Memory Approach. Springer Nature Switzerland, Cham, pp. 3–14. http://dx.doi.org/10.1007/978-3-031-57312-5_2.

Ige, A.O., Sibiya, M., 2024. State-of-the-art in 1D convolutional neural networks: A survey. IEEE Access 12, 144082–144105. http://dx.doi.org/10.1109/ACCESS.2024.3433513.

Iranzad, R., Liu, X., 2025. A review of random forest-based feature selection methods for data science education and applications. Int. J. Data Sci. Anal. 20 (2), 197–211. http://dx.doi.org/10.1007/s41060-024-00509-w.

Jakubowska, M., 2011. Signal processing in electrochemistry. Electroanalysis 23 (3), 553–572. http://dx.doi.org/10.1002/elan.201000465, URL https://analyticalsciencejournals.onlinelibrary.wiley.com/doi/abs/10.1002/elan.201000465.

Kammarchedu, V., Butler, D., Ebrahimi, A., 2022. A machine learning-based multimodal electrochemical analytical device based on eMoSx-LIG for multiplexed detection of tyrosine and uric acid in sweat and saliva. Anal. Chim. Acta 1232, 340447. http://dx.doi.org/10.1016/j.aca.2022.340447, URL https://www.sciencedirect.com/science/article/pii/S0003267022010182.

Karadag, B., Zeybekler, S.E., Gelen, S.S., Sabour-Takanlou, L., Sabour-Takanlou, M., Biray Avci, C., Odaci, D., 2025. Electrodeposition of carbon nanotubes and conjugation of arginyl-glycyl-aspartic acid for the following of glioblastoma cells on bionanocomposites. Bioelectrochemistry 164, 108937. http://dx.doi.org/10.1016/j.bioelechem.2025.108937, URL https://www.sciencedirect.com/science/article/pii/S1567539425000404.

Kim, J., Oh, S., Kim, H., Choi, W., 2023. Tutorial on time series prediction using 1D-CNN and BiLSTM: A case example of peak electricity demand and system marginal price prediction. Eng. Appl. Artif. Intell. 126, 106817. http://dx.doi.org/10.1016/j.engappai.2023.106817, URL https://www.sciencedirect.com/science/article/pii/S0952197623010011.

Kim, J., Park, M., 2021. Recent progress in electrochemical immunosensors. Biosensors 11, http://dx.doi.org/10.3390/bios11100360.

Kosicka, E., Krzyzak, A., Dorobek, M., Borowiec, M., 2022. Prediction of selected mechanical properties of polymer composites with alumina modifiers. Materials 15, http://dx.doi.org/10.3390/ma15030882.

Kumar, S., Kalkal, A., 2021. 3 - electrochemical detection: Cyclic voltammetry/differential pulse voltammetry/impedance spectroscopy. In: Khondakar, K.R., Kaushik, A.K. (Eds.), Nanotechnology in Cancer Management. Elsevier, pp. 43–71. http://dx.doi.org/10.1016/B978-0-12-818154-6.00008-1, URL https://www.sciencedirect.com/science/article/pii/B9780128181546000081.

Ladányi, A., Ladányi, A., Mukherjee, A., Kenny, H., Johnson, A., Mitra, A., Sundaresan, S., Nieman, K., Pascual, G., Benitah, S., Montag, A., Yamada, S., Abumrad, N., Lengyel, E., 2018. Adipocyte-induced CD36 expression drives ovarian cancer progression and metastasis. Oncogene 37, 2285–2301. http://dx.doi.org/10.1038/s41388-017-0093-z.

Li, X., Fu, Y.-H., Wei, N., Yu, R.-J., Bhatti, H., Zhang, L., Yan, F., Xia, F., Ewing, A.G., Long, Y.-T., Ying, Y.-L., 2024. Emerging data processing methods for single-entity electrochemistry. Angew. Chem. Int. Ed. 63 (17), e202316551. http://dx.doi.org/10.1002/anie.202316551, URL https://onlinelibrary.wiley.com/doi/abs/10.1002/anie.202316551.

Li, Y., Liu, M., Xiang, C., Xie, Q., Yao, S., 2006. Electrochemical quartz crystal microbalance study on growth and property of the polymer deposit at gold electrodes during oxidation of dopamine in aqueous solutions. Thin Solid Films 497 (1), 270–278. http://dx.doi.org/10.1016/j.tsf.2005.10.048, URL https://www.sciencedirect.com/science/article/pii/S0040609005020262.

Liao, X., Yan, S., Li, J., Jiang, C., Huang, S., Liu, S., Zou, X., Zhang, G., Zou, J., Liu, Q., 2022. CD36 and its role in regulating the tumor microenvironment. Curr. Oncol. 29, 8133–8145. http://dx.doi.org/10.3390/curroncol29110642.

Liu, L., Si, Y.-W., 2022. 1D convolutional neural networks for chart pattern classification in financial time series. J. Supercomput. 78 (12), 14191–14214. http://dx.doi.org/10.1007/s11227-022-04431-5.

Liu, N., Ye, W., Liu, G., Zhao, G., 2022. Improving the accuracy of stripping voltammetry detection of Cd2+ and Pb2+ in the presence of Cu2+ and Zn2+ by machine learning: Understanding and inhibiting the interactive interference among multiple heavy metals. Anal. Chim. Acta 1213, 339956. http://dx.doi.org/10.1016/j.aca.2022.339956, URL https://www.sciencedirect.com/science/article/pii/S000326702200527X.

Löning, M., Bagnall, A., Ganesh, S., Kazakov, V., Lines, J., Király, F., 2019. Sktime: A unified interface for machine learning with time series. arXiv arXiv:1909.07872.

Lu, C.-J., Lee, T.-S., Chiu, C.-C., 2009. Financial time series forecasting using independent component analysis and support vector regression. Decis. Support Syst. 47, 115–125. http://dx.doi.org/10.1016/j.dss.2009.02.001.

Luo, R., Qi, X., 2017. Function-on-function linear regression by signal compression. J. Amer. Statist. Assoc. 112, 690–705. http://dx.doi.org/10.1080/01621459.2016.1164053.

Marrel, A., Iooss, B., 2024. Probabilistic surrogate modeling by Gaussian process: A review on recent insights in estimation and validation. Reliab. Eng. Syst. Saf. 247, 110094. http://dx.doi.org/10.1016/j.ress.2024.110094, URL https://www.sciencedirect.com/science/article/pii/S0951832024001686.

Martínez, F., Frías, M.P., Pérez, M.D., Rivera, A.J., 2019. A methodology for applying k-nearest neighbor to time series forecasting. Artif. Intell. Rev. 1–19. http://dx.doi.org/10.1007/s10462-017-9593-z.

Miao, W., Vasile, E., Lane, W.A.S., Lawler, J., 2001. CD36 associates with CD9 and integrins on human blood platelets. Blood 97 6, 1689–1696. http://dx.doi.org/10.1182/BLOOD.V97.6.1689.

Mollarasouli, F., Kurbanoğlu, S., Ozkan, S., 2019. The role of electrochemical immunosensors in clinical analysis. Biosensors 9, http://dx.doi.org/10.3390/bios9030086.

Oishi, T., Hayashi, Y., Noguchi, M., Yano, F., Kumada, S., Takayama, K., Okada, K., Onuki, Y., 2020. Creation of novel large dataset comprising several granulation methods and the prediction of tablet properties from critical material attributes and critical process parameters using regularized linear regression models including interaction terms. Int. J. Pharm. 119083. http://dx.doi.org/10.1016/j.ijpharm.2020.119083.

Pepino, M., Kuda, O., Samovski, D., Abumrad, N., 2014. Structure-function of CD36 and importance of fatty acid signal transduction in fat metabolism. Annu. Rev. Nutr. 34, 281–303. http://dx.doi.org/10.1146/annurev-nutr-071812-161220.

Piro, B., Reisberg, S., 2017. Recent advances in electrochemical immunosensors. Sensors (Basel, Switzerland) 17, http://dx.doi.org/10.3390/s17040794.

Poon, E., Luo, X.-L., Webb, S., Yan, B., Zhao, R., Wu, S.C.M., Yang, Y., Zhang, P., Bai, H., Shao, J., Chan, C., Chan, G.C., Tsang, S., Gundry, R.L., Yang, H.-T., Boheler, K., 2020. The cell surface marker CD36 selectively identifies matured, mitochondria-rich hPSC-cardiomyocytes. Cell Res. 30, 626–629. http://dx.doi.org/10.1038/s41422-020-0292-y.

Roustaei, N., 2024. Application and interpretation of linear-regression analysis. Med. Hypothesis, Discov. Innov. Ophthalmol. J. 13 (3), 151–159. http://dx.doi.org/10.51329/mehdiophthal1506, URL https://pubmed.ncbi.nlm.nih.gov/39507810, Review; eCollection 2024 Fall.

Saeed, A., Ozcelebi, T., Lukkien, J., 2019. Multi-task self-supervised learning for human activity detection. Proc. ACM Interact. Mob. Wearable Ubiquitous Technol. 3 (2), http://dx.doi.org/10.1145/3328932.

Sapountzoglou, N., Lago, J., Raison, B., 2020. Fault diagnosis in low voltage smart distribution grids using gradient boosting trees. Electr. Power Syst. Res. http://dx.doi.org/10.1016/j.epsr.2020.106254.

Setiawan, H., Tampati, I.F., Putra, I.G.M., Girinoto, 2024. Optimization of MLP-regressor for predicting student's cumulative grade point average (GPA). In: 2024 4th International Conference of Science and Information Technology in Smart Administration. ICSINTESA, pp. 628–633. http://dx.doi.org/10.1109/ICSINTESA62455.2024.10747977.

Silverstein, R., Febbraio, M., 2009. CD36, a scavenger receptor involved in immunity, metabolism, angiogenesis, and behavior. Sci. Signal. 2, re3. http://dx.doi.org/10.1126/scisignal.272re3.

Suganyadevi, M., Babulal, C., 2014. Support vector regression model for the prediction of loadability margin of a power system. Appl. Soft Comput. 24, 304–315. http://dx.doi.org/10.1016/J.ASOC.2014.07.015.

Sumorek, M., Idzkowski, A., 2023. Time series forecasting for energy production in stand-alone and tracking photovoltaic systems based on historical measurement data. Energies http://dx.doi.org/10.3390/en16176367.

Sun, H., Burton, H., Huang, H., 2021. Machine learning applications for building structural design and performance assessment: State-of-the-art review. J. Build. Eng. 33, 101816. http://dx.doi.org/10.1016/J.JOBE.2020.101816.

Teng, Y., Li, W., Gunasekaran, S., 2023. Biosensors based on single or multiple biomarkers for diagnosis of prostate cancer. Biosens. Bioelectron.: X http://dx.doi.org/10.1016/j.biosx.2023.100418.

Valente, J., Maldonado, S., 2020. SVR-FFS: A novel forward feature selection approach for high-frequency time series forecasting using support vector regression. Expert Syst. Appl. 160, 113729. http://dx.doi.org/10.1016/j.eswa.2020.113729.

Valkenborg, D., Rousseau, A.-J., Geubbelmans, M., Burzykowski, T., 2023. Support vector machines. Am. J. Orthod. Dentofacial. Orthop. 164 (5), 754–757. http://dx.doi.org/10.1016/j.ajodo.2023.08.003.

Vanneschi, L., Silva, S., 2023. Decision tree learning. In: Lectures on Intelligent Systems. Springer International Publishing, Cham, pp. 149–159. http://dx.doi.org/10.1007/978-3-031-17922-8_6.

Wang, J., Li, B., Li, Z., Ren, K., Jin, L., Zhang, S., Chang, H., Sun, Y., Ji, J., 2014. Electropolymerization of dopamine for surface modification of complex-shaped cardiovascular stents. Biomaterials 35 (27), 7679–7689. http://dx.doi.org/10.1016/j.biomaterials.2014.05.047, URL https://www.sciencedirect.com/science/article/pii/S0142961214006048.

Wang, Z., Wang, P., Liu, K., Wang, P., Fu, Y., Lu, C.-T., Aggarwal, C.C., Pei, J., Zhou, Y., 2024. A comprehensive survey on data augmentation. arXiv:2405.09591, URL https://arxiv.org/abs/2405.09591.

Wang, Z., Wang, Y., Zeng, R., Srinivasan, R., Ahrentzen, S., 2018. Random forest based hourly building energy prediction. Energy Build. http://dx.doi.org/10.1016/J.ENBUILD.2018.04.008.

Wen, Q., Sun, L., Yang, F., Song, X., Gao, J., Wang, X., Xu, H., 2021. Time series data augmentation for deep learning: A survey. In: Proceedings of the Thirtieth International Joint Conference on Artificial Intelligence. In: IJCAI-2021, International Joint Conferences on Artificial Intelligence Organization, pp. 4653–4660. http://dx.doi.org/10.24963/ijcai.2021/631.

Wistuba, M., Schilling, N., Schmidt-Thieme, L., 2017. Scalable Gaussian process-based transfer surrogates for hyperparameter optimization. Mach. Learn. 107, 43–78. http://dx.doi.org/10.1007/s10994-017-5684-y.

Xia, N., Gao, F., Zhang, J., Wang, J., Huang, Y., 2024. Overview on the development of electrochemical immunosensors by the signal amplification of enzyme- or nanozyme-based catalysis plus redox cycling. Molecules 29, http://dx.doi.org/10.3390/molecules29122796.

Zeybekler, S.E., Odaci, D., 2023. Carbon nanotube-incorporated nanofibers for immunosensor preparation against CD36. ACS Omega 8, 5776–5786. http://dx.doi.org/10.1021/acsomega.2c07458.

Zhang, H., Cissé, M., Dauphin, Y., Lopez-Paz, D., 2017. mixup: Beyond empirical risk minimization. arXiv arXiv:1710.09412.

Zhang, B., Zhang, Y., Shen, J., Zhou, Z., Zhu, G., 2024. Research on differential pulse voltammetry detection method for low concentration glucose based on machine learning model. Int. J. Electrochem. Sci. 19 (2), 100479. http://dx.doi.org/10.1016/j.ijoes.2024.100479, URL https://www.sciencedirect.com/science/article/pii/S1452398124000208.

Zhou, T., Peng, Y., 2020. Kernel principal component analysis-based Gaussian process regression modelling for high-dimensional reliability analysis. Comput. Struct. http://dx.doi.org/10.1016/j.compstruc.2020.106358.

Zhou, Z., Wen, C., Yang, C., 2016. Fault isolation based on k-nearest neighbor rule for industrial processes. IEEE Trans. Ind. Electron. 63, 2578–2586. http://dx.doi.org/10.1109/TIE.2016.2520898.